Faraday Discussions

Cite this: *Faraday Discuss.*, 2016, **187**, 555

PAPER

View Article Online
View Journal | View Issue

High spatial resolution (1.1 μm and 20 nm) FTIR polarization contrast imaging reveals pre-rupture disorder in damaged tendon

Richard Wiens,[a] Catherine R. Findlay,[a] Samuel G. Baldwin,[b] Laurent Kreplak,[b] J. Michael Lee,[cd] Samuel P. Veres[ce] and Kathleen M. Gough*[a]

Received 15th November 2015, Accepted 11th January 2016
DOI: 10.1039/c5fd00168d

Collagen is a major constituent in many life forms; in mammals, collagen appears as a component of skin, bone, tendon and cartilage, where it performs critical functions. Vibrational spectroscopy methods are excellent for studying the structure and function of collagen-containing tissues, as they provide molecular insight into composition and organization. The latter is particularly important for collagenous materials, given that a key feature is their hierarchical, oriented structure, organized from molecular to macroscopic length scales. Here, we present the first results of high-resolution FTIR polarization contrast imaging, at 1.1 μm and 20 nm scales, on control and mechanically damaged tendon. The spectroscopic data are supported with parallel SEM and correlated AFM imaging. Our goal is to explore the changes induced in tendon after the application of damaging mechanical stress, and the consequences for the healing processes. The results and possibilities for the application of these high-spatial-resolution FTIR techniques in spectral pathology, and eventually in clinical applications, are discussed.

1. Introduction

We are using FTIR polarization contrast imaging (PCI) to examine mechanically damaged mammalian tendon. Characteristic features in the polarized FTIR spectra of collagen were recognized early in the development of infrared bio-spectroscopy,[1,2] even before the true triple helix molecular architecture had been discovered.[3–5] The polarization dependence results from the highly ordered arrangement of the basic units (tropocollagen) and their alignment within the

[a]*Department of Chemistry, University of Manitoba, Winnipeg, MB, R3T 2N2, Canada. E-mail: Kathleen.Gough@umanitoba.ca*
[b]*Department of Physics and Atmospheric Science, Dalhousie University, Halifax, NS, B3H 4R2, Canada*
[c]*School of Biomedical Engineering, Dalhousie University, Halifax, NS, B3H 3J5, Canada*
[d]*Department of Applied Oral Sciences, Dalhousie University, Halifax, NS, B3H 4R2, Canada*
[e]*Division of Engineering, Saint Mary's University, Halifax, NS, B3H 3C3, Canada*

aggregated structures of the microfibrils, fibrils and fibres.[6] The complex, hierarchical architecture of collagen facilitates a multitude of specialized, highly localized functions in tissues including tendon, skin, cartilage, ligament, scar tissue and bone. Under polarized infrared light, functional groups are vibrationally excited only when the alternating dipole change of the vibration is aligned with the polarization of the incident field. Vibrational spectroscopy has been an important technique for studying these tissues, providing molecular information on composition, orientation, post-translational modification and disease.[7–11]

Collagen fibrils are the fundamental load-bearing constituent of mammalian tissues. They are approximately 50–500 nm in diameter but can be mm in length.[12] Fibrils form as self-assembled linear aggregates of tropocollagen molecules (300 nm long × 1.5 nm in diameter); the latter consist of three helical chains wound together in a triple super-helix, stabilized by interchain hydrogen bonds.[13] Our knowledge of the molecular changes occurring within overload-damaged fibrils remains sparse. Using very high magnification SEM (100 000×), Veres and Lee showed that both ruptured[14] and cyclically overloaded[15,16] bovine tendons contain collagen fibrils with "discrete plasticity": a characteristic damage morphology where discrete strain-induced kinks appear serially along the length of the nanoscale fibrils. Enzymatic probes and differential scanning calorimetry showed that some collagen molecules had undergone denaturation, *i.e.* uncoiling of the triple helix within fibrils that experienced discrete plasticity. This work led to the hypothesis that a molecular-based toughening mechanism is implicit in the structure of the mammalian collagen fibril. Our current hypothesis is that under discrete plasticity a designated subset of molecules within fibrils denature on overload, absorbing mechanical strain energy at many discrete locations along each fibril's length. Discrete plasticity in tendons may represent a naturally evolved, built-in, toughening design that is ultimately protective against actual tendon rupture.

Our goal is to obtain a molecular spectroscopic basis for understanding changes to the molecular structure of collagen fibrils, under mechanical overload injury. To that end, using a bovine tail tendon model in which overload-induced discrete plasticity damage has been well characterized,[14–16] we have studied matched-pair control and overloaded tendons with high-magnification FTIR PCI, confirming results with SEM and AFM. The highest spatial resolution far-field FTIR was attained at the IRENI beamline (Synchrotron Radiation Center, WI, now decommissioned) employing a Focal Plane Array (FPA) detector, to give 0.54 × 0.54 μm^2 pixels.[17] The Agilent high-magnification system used in the present work achieves the next best spatial resolution of 1.1 μm pixel dimension,[18] considered to be the practical limit for mid-IR with FPA.[19] This scale was sufficient to capture the orientation of bundled fibrils with fibres, including generalized sub-micron disorder, but could not provide sub-micron detail. To address the detection of finer details, single fibrils of the order of 300 nm in diameter were prepared from control tendon and examined with infrared near-field scattering scanning microscopy IR s-SNOM, at 20 nm spatial resolution. These experiments were performed with synchrotron source IR at the Advanced Light Source (ALS), Berkeley CA[20] and with a broadband mid-infrared nano-FTIR spectroscopy laser at Neaspec, GmbH, DE.[21–24] Additionally, near-field images were recorded at Neaspec using a mid-IR Quantum Cascade Laser (QCL). We show here that, regardless of source and system, PCI can be exploited in each case to reveal crucial aspects of

organization in fibres and in fibrils. The potential for spectropathological and clinical applications will be discussed.

2. Methods

2.1 Tissue collection & mechanical damage procedure

Four tendons were dissected from the tails of two young adult steers killed for food at a local abattoir (Reid's Meats, Wolfville, NS, Canada). Once removed, tendons were immediately stored at 4 °C in phosphate-buffered saline (PBS) containing 1% antibiotic/antimycotic solution (10 000 units penicillin, 10 mg streptomycin, and 25 μg amphotericin B per mL; product A5955, Sigma-Aldrich Canada). Prior to the mechanical damage procedure, a 15 mm-long sample was removed from each tendon to serve as an unloaded control. Using a servo-hydraulic materials testing system, the remainder of each tendon was subjected to 5 cycles of subrupture overload at a strain rate of 1% per s, as described previously.[15] After the mechanical damage procedure, both the control and overloaded portions of each tendon were cut in half longitudinally yielding two sets of matched-pair samples, one set for SEM, and one set for FTIR. The tendon segments, approximately 10 mm long by 4 mm in diameter, were stored at room temperature for 24 hours in PBS containing 1% antibiotic/antimycotic solution and 1% protease inhibitor (2 mM 4-(2-aminoethyl)benzenesulfonyl fluoride, 14 μM E-64, 130 μM bestatin, 1 μM leupeptin, 0.3 μM aprotinin, and 1 mM EDTA; product S8820, Sigma-Aldrich Canada) prior to preparation for SEM and FTIR spectroscopy.

2.2 Scanning electron microscopy

In preparation for SEM, matched-pair control and overloaded tendon samples were fixed for one hour in 2.5% SEM-grade glutaraldehyde, rinsed in deionized water, dehydrated in graded ethanol, and critical point dried. The tendon samples were mounted on stubs using carbon tape with their exposed internal surfaces facing upward, and then sputter-coated with gold–palladium. Imaging was conducted with a Hitachi S-4700 scanning electron microscope operating at 3 kV, 15 μA.

2.3 FTIR sample preparation and imaging at normal (5.5 μm) and high (1.1 μm) magnification pixel size

The other matched-pair set, comprising 4 matched pairs of control and mechanically overloaded tendon, that is two pairs from each animal, were shipped overnight to the University of Manitoba, immediately removed from PBS medium, covered with OCT [Sakura Finetek Inc. USA], frozen in isopentane cooled in liquid N_2, and stored at −80 °C. Cryosections were cut to 5 or 8 μm thickness at −21 °C, mounted on BaF_2 windows and refrigerated overnight at 4 °C.[25]

Nine sections from the 4 control tendon samples and ten sections from the matching 4 overloaded tendon samples were imaged with an Agilent Cary 670 interferometer and 620 infrared microscope, equipped with a 64 × 64 FPA. Normal and high magnification optics (5.5 × 5.5 μm^2 and 1.1 × 1.1 μm^2 pixels, respectively)[18] were used to explore fibril organization. Sections were typically aligned on the stage such that the fibril direction was horizontal in the field of view. Spectral acquisition and data processing were accomplished with the

ResolutionsPro FTIR spectroscopy software (Agilent Inc. version 5.2.0). All spectra were acquired as sums of 128 scans ratioed against a background of 512 scans. Initial survey images with normal magnification were conducted on one matched pair, with no, 0° or 90° polarization, where 90° corresponds to the horizontal direction of the overall fiber orientation. The majority of the study was conducted with high magnification optics. Of these, 46, 40 and 124 individual FPA tiles were acquired from control tendon sections with no, 0° and 90° polarization, respectively; similarly, 36, 64 and 212 tiles were acquired from overload tendon sections. Some sections on BaF_2 windows were stored in a sealed container at 4 °C pending re-imaging with FTIR PCI or other analyses.

The amide I and II bands differ in intensity, as they arise from different vibrational modes that produce different intrinsic changes in molecular dipole. Moreover, they change with orientation relative to the polarization of the incident IR light. The FTIR PCI false colour images were created from the ratio of amide II to amide I integrated band areas, to compensate for differences in tissue thickness across a section. Integrated band areas for amide I were taken between 1675 and 1645 cm^{-1}, and for amide II between 1567 and 1537 cm^{-1}. The baseline was established from the average in the non-absorbing region between 1790 and 1760 cm^{-1} for both. Instrumental illumination differs under the different polarizations and a new background had to be recorded in each case, necessitating slightly different colour scales. Display limits were chosen to consistently illustrate variation in orientation: 0.1 to 1.3 for all 0° images; 0.6 to 2.0 for all 90° images, 0.6 to 1.2 for images acquired without the polarizer accessory. These scales were chosen such that a ratio of 1.0 represented spectra wherein the amide I and II bands also had approximately equal height, while the range of the false colours was primarily aqua-blue to yellow-green for normal tissue. Extremes are reached only when fibers within the field of view are strongly aligned with or against the polarization.

2.4 AFM imaging

Following the FTIR imaging experiments, two of the overload tendon sections were returned for AFM surface analysis at the Structural Nanomechanics Lab (Dalhousie University). Each section was imaged in air with a Bioscope Catalyst AFM (Bruker, USA) mounted on an Olympus IX71 inverted microscope (Olympus, USA). ScanAsyst Fluid probes (Bruker, USA) with a nominal cantilever spring constant of 0.7 N m^{-1} were used. The AFM was operated in peak force quantitative nanomechanical mapping mode at a scan rate of 0.5 to 1 Hz. The images were processed in Nanoscope Analysis (Bruker, USA) or SPIP (Image Metrology, Denmark). To ensure that areas being measured corresponded to those imaged with FTIR PCI, a stack of survey images were taken at 25 nm spatial resolution over 40 or 50 μm regions, and the morphology was matched to the IR and visible images. Higher resolution images (10 μm region, 10 nm spatial resolution) were obtained on selected regions.

2.5 Fibril preparation for AFM and nanoscale near-field IR

In order to conduct preliminary nanoscale near-field IR analysis of collagen fibrils, an additional tail tendon was acquired from a different young adult steer. The tendon was laid flat between sheets of gauze moistened with PBS, double

bagged, and stored at −86 °C. After thawing at room temperature in its sealed bag, the tendon was rinsed in deionized water and dissected further using tweezers and a fine-tipped glass rod in 1 mL of deionized water until the mixture appeared cloudy. A 50 μL drop of the suspension was deposited on a 1 cm^2 gold-coated silicon wafer, allowed to settle for 10 min, rinsed with deionized water and dried with nitrogen. Visible images at 100× and 50× were used to identify single collagen fibrils prior to the first nano-FTIR experiments at the ALS, Berkeley CA.

ALS data collection. As per the standard protocol for mounting samples at Beam Line 5.4.1, ALS, the Au wafer was taped onto a magnetic mount, inserted within the chamber and manually adjusted to position the desired target into the field of view. The specially modified AFM (Innova, Bruker), and the source, detector and various optics were manually adjusted to acquire AFM images and Synchrotron Infrared NanoSpectroscopy (SINS) spectra.[20] Visible and AFM images revealed a multitude of residual fibres and fibrils; two fibrils with cross sections of the order of 300 nm were selected. Spectra were recorded with a modified commercial rapid-scan FTIR spectrometer (Nicolet 6700, Thermo-Scientific), with an asymmetric Michaelson interferometer. The second order amplitude ($s(\omega)$) and phase ($\varphi(\omega)$) spectra for the backscattered light were recorded at locations on and off the fibrils. For each background and sample, 512 scans were co-added, with a spectral data spacing of 8 cm^{-1}. Only 2 or 3 good quality spectra could be acquired per hour, since a background scan was required at least once every two hours, and 20 minutes was required to record individual spectra with sufficient signal-to-noise ratios. Post-processing custom programs with commercial fast Fourier transform analysis packages (Wavemetrics Igor) developed in-house at BL 5.4.1, ALS were used to convert the scattering data to a format that corresponds to an IR absorbance spectrum, see below.[20]

Neaspec data collection. The same two fibrils were examined with a scattering Scanning Near-Field Optical Microscope, sSNOM, with the broadband mid-IR nano-FTIR illumination unit from Neaspec.[21–24] In the first experiment, spectra were obtained by tuning the laser through three spectral ranges (800–1200 cm^{-1}, 1200–1800 cm^{-1} and 1800–2100 cm^{-1}), again recording the second order amplitude, $s(\omega)$, and phase, $\varphi(\omega)$, spectra for the backscattered light at locations on and off the fibril. Spectra were recorded with a full-optical travel range of 800 μm, which results in a real frequency resolution of 12.5 cm^{-1}. Zero-filling was added, reducing the frequency spacing of the data points to 3.125 cm^{-1}. Following standard post-processing, below,[21–24] similar to that performed on the ALS data, the mid-IR absorption spectra were assembled from the three spectral segments. In the second experiment, images were obtained across one of the fibrils by scanning the entire area at on- and off-resonant wavelengths, 1655 cm^{-1} and 1850 cm^{-1}, respectively, at 5 nm intervals, though with an anticipated 20 nm spatial resolution. Full spectra were recorded in about 3.5 minutes; single wavelength images were recorded at 20 ms per pixel over 100 × 200 pixels area, in less than 7 minutes per image. The amplitude and phase images showed that a minor shift in position occurred between the two acquisitions. After export to MatLab, the array from the 1655 cm^{-1} scan was shifted down one row and over three rows (5 nm and 15 nm) to achieve correct image registration of the single wavelength data files before creation of ratioed images.

Post-processing of near-field data. In each of the near-field experiments, amplitude, $s_2(\omega)$, and phase $\varphi_2(\omega)$ spectra were obtained from the imaginary function of the complex-valued second order scattering coefficient, (σ_2),[22,24] according to the relationship:

$$\sigma_2(\omega) = s_2(\omega)e^{i[\varphi(\omega)]} \quad (1)$$

The near-field nano-FTIR absorbance spectrum is obtained by normalizing the signal on a fibril against a signal from on a flat, non-absorbing surface, here, a nearby point on the gold-coated wafer:

$$\mathrm{Im}\{\sigma_2(\omega)\} = \mathrm{Im}\left\{\frac{s_{2\ (\mathrm{fibril},\omega)}}{s_{2\ (\mathrm{Au},\omega)}} e^{i[\varphi(\mathrm{fibril},\omega)-\varphi(\mathrm{Au},\omega)]}\right\} = \frac{s_{2\ (\mathrm{fibril},\omega)}}{s_{2\ (\mathrm{Au},\omega)}}\sin[\varphi(\mathrm{fibril})-\varphi(\mathrm{Au})] \quad (2)$$

Single wavelength images recorded with the QCL source yielded amplitude and phase results that could be displayed in several formats: individual, normalized, or as the ratio of the near-field absorbance signals at 1655 and 1850 cm^{-1}.

3. Results

The infrared spectrum of normal, undamaged tendon (Fig. 1A) displays the numerous well-known spectral features that are unique to collagen assemblies,[26–28] and derive from the unusual molecular composition and superhelical structure. In each of the three α-chains that form a tropocollagen molecule, the repeat amino acid sequence is Gly–X–Y, where X and Y are often proline and hydroxyproline, respectively.[29] The alignment is such that the carbonyls are nearly perpendicular to the direction of the backbone; this orientation is retained to a significant extent in the assemblies. The intensity of the amide I band at 1660 cm^{-1} is enhanced when light is polarized parallel to carbonyl (0°); all other bands, particularly the amide II at 1545 cm^{-1}, are enhanced under light polarized

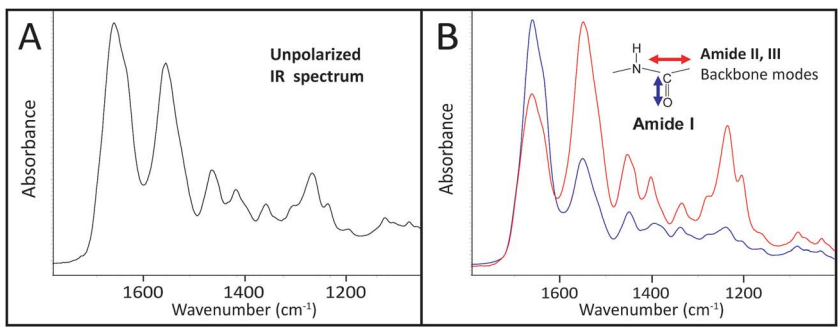

Fig. 1 Single-pixel FTIR spectra of control tendon extracted from FPA images acquired at normal magnification optics, 5.5 μm, illustrate the many potential spectral markers for fibril orientation. Spectra are shown (A) without polarizer (B) with polarizer oriented at 0° (blue, enhanced C=O stretch at 1660 cm^{-1}) and 90° (red, enhanced C–N stretch at 1545 cm^{-1} and backbone modes). Spectra are normalized to the stronger band in each case.

parallel to the fibril direction (90°), Fig. 1B. These spectral features can be easily exploited to reveal fibril orientation under polarized infrared light, *provided* that the internal organization has been retained at a molecular level. The contrast would be reduced by fibril disorganization and/or molecular denaturation.

The SEM images of collagen fibrils before and after tendon overload, and a typical series of stress–strain curves for tendon during sub-rupture overload, are shown in Fig. 2. Fibrils from control tendon exhibit the expected D-banding[5,14,30,31] that arises from the regular staggered arrangement of tropocollagen molecules within the fibrils, Fig. 2A. The interpretation of such stress–strain curves (Fig. 2B) is provided in detail elsewhere.[6,15,32] Briefly, under the application of low force to the tendon sample, out to ~0.1 strain in Fig. 2B, the 100 μm-scale collagen fibre crimp in the tissue straightens (see Fig. 3–5). If the extending force were removed, this crimp would reform as the tissue retracted. Beyond 0.1 strain, the collagen fibres are in direct tension, loading more or less elastically, and the stress–strain curve is linear. Sub-rupture overload is achieved by application of sufficient force to extend the tendon into the final non-linear region, beyond the yield stress point, (σ_y, Fig. 2B). In our sub-rupture experiments, the tendon sample was extended until the slope of the stress/strain curve became zero (~0.3 strain in the first overload cycle), and the extension was reversed to zero. This process was performed 5 times. Under cyclic overload, plastic damage accumulates in the tendon and greater final strain is achieved—with a smaller maximum force—in the four subsequent overload cycles.

SEM imaging of matched-pair control and overload samples confirmed that discrete plasticity damage was produced by repeated stretching beyond the tendon's yield point. As previously observed,[14,15] fibrils with discrete plasticity were characterized by the presence of kinks that repeated along the length of fibrils with nanoscale frequency, while some kinked fibrils also had a surface layer of denatured collagen, masking the fibrils' native D-banding (Fig. 2C).

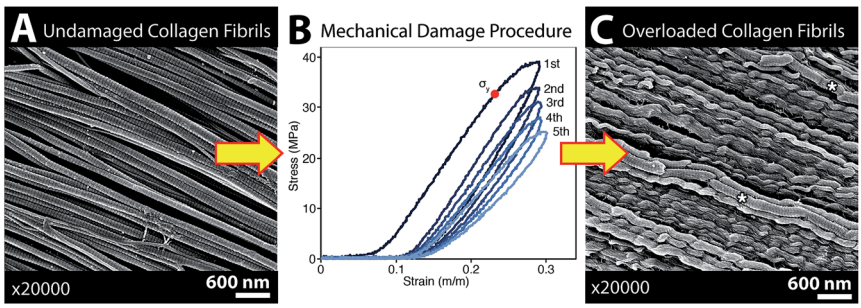

Fig. 2 SEM imaging confirmed that the subrupture overload procedure produced discrete plasticity damage in the tendon samples used for spectroscopic analysis. (A) SEM of a native, unloaded control tendon showing the normal straight, D-banded appearance of collagen fibrils. (B) Typical stress–strain curves showing 5 cycles of subrupture overload, where the tendon is repeatedly stretched beyond its yield point, σ_y. (C) SEM of fibrils with longitudinally repeating kinks called discrete plasticity damage. Some fibrils with discrete plasticity retain their D-banding (* in (C)), while in other kinked fibrils the D-banding is obscured by a surface layer of denatured collagen. Note that in the marked fibrils (* in (C)) distortion of the D-banding is an imaging artefact.

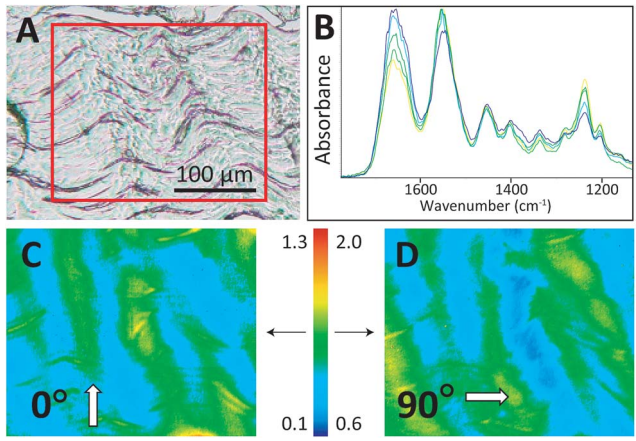

Fig. 3 The control tendon exhibits a normal crimp pattern under visible and polarized illumination. (A) White light 10× photoimage of a control tendon section on a BaF_2 window. The red box outlines the area examined with FTIR PCI (4 × 3 FPA tiles). (B) Spectra extracted from FTIR PCI mosaics to show variation observed under polarization at (C) 0° and (D) 90°. The false colour bar indicates the range of amide II to amide I band area values for (C) and (D), as described in Methods; the arrows indicate the image to which numerical scale applies.

The four control/overload sample pairs matching the set imaged with SEM were cryosectioned and imaged in FTIR transmission mode with normal and high magnification optics. The fibres of all control tendons exhibited the expected

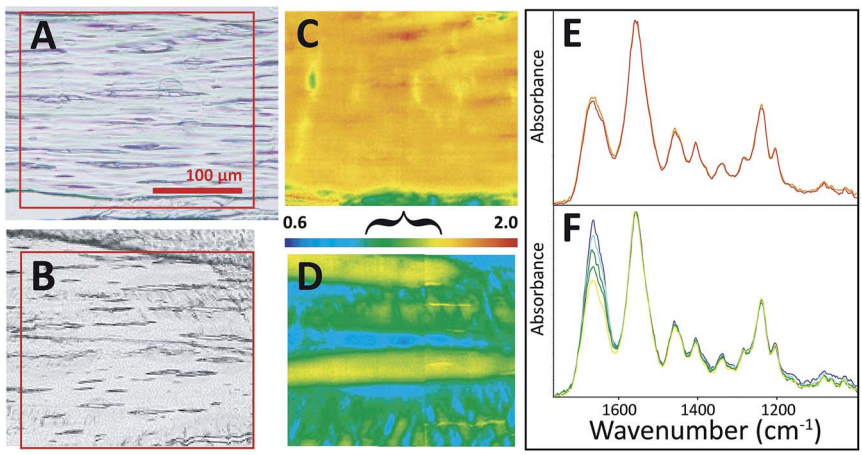

Fig. 4 FTIR PCI revealed sub-micron disorder in some stressed tendons. Visible images of tendon sections on BaF_2 windows show (A) loss of crimp structure on some sections and (B) residual crimp structure in other sections. FTIR PCI at 90° showed (C) a high degree of molecular alignment with fibrils in the case of uniform stretch and (D) alternating regions of alignment and crimp in the case of non-uniform stretch. Spectra extracted from FTIR images corresponding to the range of colours in FTIR PCI are shown in (E) and (F), normalized to amide II band. False colour scale bar as in Fig. 3 for 90°; the bracket indicates a range typical of normal crimped tendon. Spectra shown represent the full range of relative intensities observed.

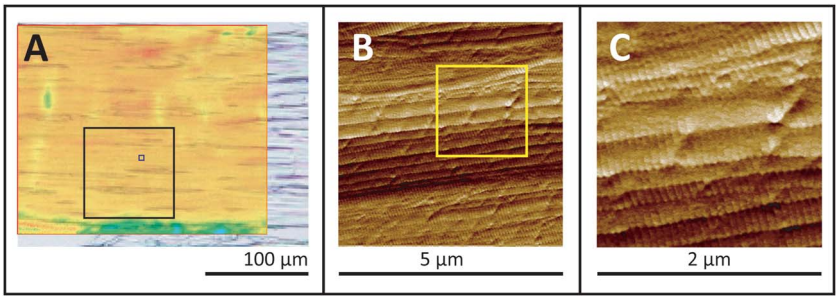

Fig. 5 Uniformly stressed tendon is lightly kinked. (A) The semi-transparent FTIR PCI false colour image from Fig. 4C is superimposed on a visible image. Black boxes outline the locations of 100 × 100 μm^2 (results not shown) and 5 × 5 μm^2 AFM images; (B) AFM 5 × 5 μm^2 image recorded at 10 nm resolution. (C) 2 × 2 μm^2 region as outlined by yellow box (B), enlarged to facilitate identification of low kink density in the otherwise normal, intact D-banded fibrils.

microscale crimps under white light (Fig. 3A), with an undulation repeat of about 100–150 μm. Note that this naturally occurring crimp pattern is 1000-fold greater than the nanokinks that are produced by mechanical damage within the individual fibrils that comprise the microscopic fibre bundles. Spectra were extracted from mosaic images, acquired as FTIR PCI with high magnification optics, and displayed at full scale to clarify the variation in the ratio of the integrated band areas of amide I and II with fibril orientation (Fig. 3B). The false colour scales in the processed images were adjusted separately for parallel and perpendicular polarizations to yield complementary images for perpendicular (0°) and parallel (90°) polarizations (Fig. 3C and D), as described in the Methods section. The high magnification optics images have sufficient spatial resolution to show that control tendon exhibits the expected polarization dependence, wherein the visible crimped appearance of the well-organized fibres is reflected in the FTIR PCI images. The colours in Fig. 3B match the colours in the processed images. For the example shown, the crimps only become parallel to the 90° light at the top of the wave, yellow spectrum and yellow regions in (Fig. 3B and C).

All tendons subjected to sub-rupture overload stress lost the characteristic undulating crimps, but not uniformly. In some regions, the fibres were visibly straightened under white light (Fig. 4A), but other sections appeared to have retained crimped regions (Fig. 4B). FTIR PCI at 90° mirrored the organization in the visible images in the first case (Fig. 4C and D). Spectra uniformly showed significantly enhanced amide II C–N stretch backbone modes across the section; the amide II to amide I ratio reached the high end of the false colour scale, yellow-red, as illustrated in the images (Fig. 4A, C and E). In the second example, where some crimp structure was retained, the ratios of the band areas were within normal bounds, translating as blue-green-yellow (Fig. 4B, D and F), implying that the tendon had undergone less, albeit uneven, stress during overload. However, closer analysis of the spectra from this FTIR PCI revealed differences strongly suggestive of disorder at a molecular scale: the enhancement of the amide II was much less than expected in regions that visibly appeared to be straight and uncrimped, along the deeper blue horizontal swaths (*vide infra*).

To confirm this interpretation, the two overload samples shown in Fig. 4 were returned for AFM imaging of the regions of interest in the tissue. Results of this correlated imaging are shown in Fig. 5 and 6. Part of the FTIR PCI false colour image has been rendered semi-transparent to allow visual inspection of the macroscopic axial alignment. All the AFM pictures are peak-force error channels, chosen to emphasize the finest details in the topography as well as the edges of individual fibrils. As seen in Fig. 5A, the orientation of the AFM images of the first sample matched that of the FTIR PCI. AFM images acquired at 25 nm (data not shown) and 10 nm resolution allowed detection of discrete plasticity, with the kinks along individual fibrils, spaced at ~800 nm intervals.

The second sample was not precisely aligned to match the FTIR PCI and AFM images, Fig. 6A, but this does not impact the analysis. A series of 40 μm survey AFM images were acquired at 25 nm spatial resolution inside the yellow rectangle (data not shown). Three of six higher-magnification AFM images are shown at two enlargement scales (Fig. 6B and C), showing aligned, moderately kinked fibrils in the top image and a progressively more disordered arrangement of kinked fibrils in the middle and lower images. The uppermost AFM image in Fig. 6C is similar to those in Fig. 5. The progressively disordered regions correspond to the regions revealed by FTIR PCI to contain submicron disorder, that is, a loss of axial alignment at the fibril or molecular scale (blue-green regions in false colour image, Fig. 6A).

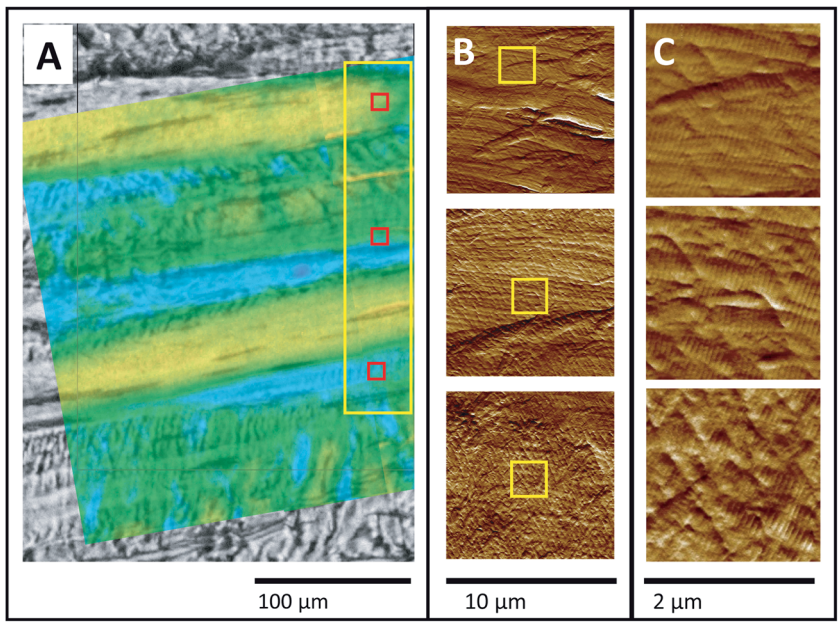

Fig. 6 Non-uniformly stressed tendon. (A) Visible image of tendon with semi-transparent FTIR PCI false colour image from Fig. 4C superimposed. The large yellow rectangle outlines the location of lower-resolution AFM images, taken as a series of 40 × 40 μm^2 areas (not shown). (B) Three 10 × 10 μm^2 AFM images, recorded at 10 nm spatial resolution at red squares in (A). (C) Excerpts from (B), outlined by yellow squares, enlarged to facilitate identification of kinking in the otherwise normal, intact D-banded fibrils.

The first Synchrotron Infrared NanoSpectroscopy (SINS) spectra from a control collagen fibril, recorded at ALS, are presented in Fig. 7A. The AFM image on the left was acquired rapidly in order to locate a useful target, and shows parts of two normal fibrils. Following Fourier transform of the second order scattered near-field light,[20] the nano-FTIR absorption spectra, Im $\sigma_2(\omega)$ are obtained. These match well with the far-field IR spectrum of collagen shown in Fig. 1. The proline ring mode ($\sim$1465 cm^{-1}) is just barely visible. Similar results were obtained on the same fibrils and locations from second order backscattering using the broadband nano-FTIR illumination source from Neaspec (Neaspec, GmbH, DE), shown beside the synchrotron spectra. The nano-FTIR absorption spectra are very similar to the results from ALS; the proline ring mode is clearly identifiable. The ALS spectra are noisier but should not be compared directly, since the Neaspec data were zero-filled.

Single wavelength images were acquired with the Neaspec QCL at the amide I maximum (1655 cm^{-1}), and at a non-absorbing wavelength (1850 cm^{-1}), Fig. 7B. The area was scanned in 5 nm steps, where the expected spatial resolution is 20 nm. All amplitude and phase images show the fibril features. The on- and off-resonance contrast in amplitude is much less than the contrast in phase, but both

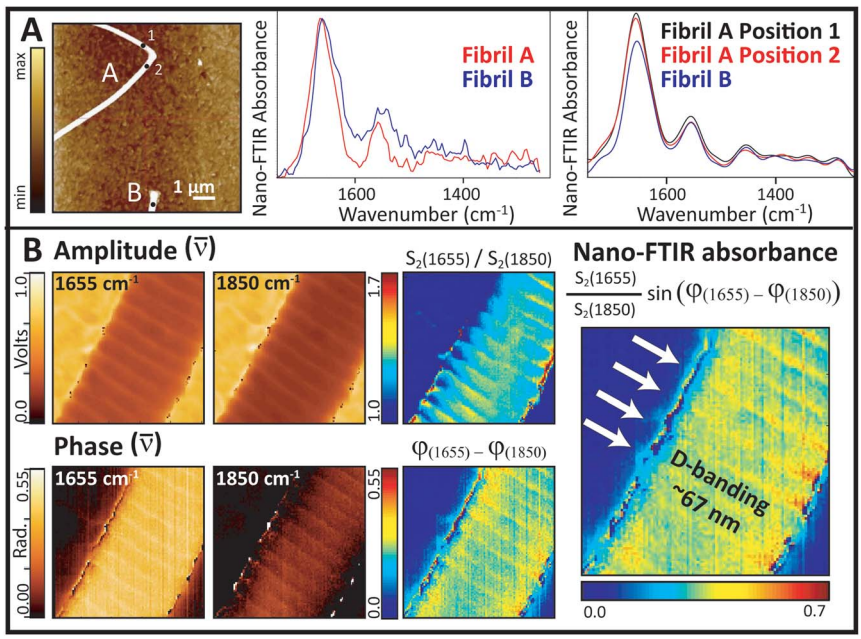

Fig. 7 Synchrotron Infrared NanoSpectroscopy (SINS) and infrared QCL s-SNOM of collagen fibrils demonstrate that fibril organization can be examined at nanoscale spatial resolution. (A) Mid-IR spectra from single points: (Left) AFM height image of the target fibrils (256 lines sampled at 512 points per line), at ALS, Berkeley USA; (Center) post-processed near-field nano-FTIR spectra (aka SINS). (Right) similar spectra acquired at points indicated by black dots, using the broadband nano-FTIR illumination source from Neaspec (Neaspec, GmbH, DE). (B) (Left) single wavelength QCL amplitude and phase images at 1655 and 1850 cm^{-1}. (Center) normalized amplitude and phase images. (Right) relative near field nano-FTIR absorbance intensity shows D-banding.

parts are required to construct the relative near-field FTIR absorbance image. The highest contrast seen at the edges of the fibril probably arises from artefacts in the edge scatter. The D-banding at ~67 nm spacing is well-resolved in all images, indicating a strong difference in optical response. The alteration in intensity arises from the gap-overlap regions caused by molecular stagger in the fibrils, just as would be seen in an SEM image.

4. Discussion

A little over a decade ago, a Faraday Discussion meeting was held to consider the state-of-the-art applications of spectroscopy in biomedicine. At that time, the state-of-the-art for FTIR spectroscopic imaging required a synchrotron source, and the highest spatial resolution possible was defined by the wavelength-dependent diffraction limit, from 10 to 2.5 μm.[33] Recent advances have made dramatic improvements on those limitations: benchtop FTIR instruments that can be used for spectropathology, with the necessary speed, sensitivity and high spatial resolution, are now commercially available. The diffraction limit to spatial resolution has been broken with near-field IR, allowing us to probe areas of the order of a few nanometers, in several different instrumental designs.[20,22] Here, we present results that employ all of these advances: (1) far-field diffraction-limited FTIR microscopy with a thermal bench source and improved optics that yield 1.1 μm pixels,[18] further enhanced with polarization contrast and (2) near-field FTIR with 20 nm resolution, with a synchrotron source FTIR[20] and with broadband nano-FTIR illumination source.[21–24] Our purpose is to illustrate the advantages these technological advances can bring to spectropathology, and eventually to clinical pathology in the context of our on-going study of mechanical damage and healing in tendons. We will first summarize what we have learned from high-magnification transmission FTIR PCI and from near-field IR imaging in the present study, and then consider larger implications for spectropathological and clinical applications.

4.1 What does high-magnification far-field infrared imaging tell us?

FTIR imaging analysis of control and mechanically overloaded tendon section, with polarization contrast, allows us to identify regions where axial alignment of the fibrils has been lost. We interpret this as a spectroscopic proxy for discrete plasticity kinking. These results demonstrate that we can now evaluate mechanically-induced damage in tendon sections, at an unprecedented, physically relevant length scale. We can thus study the changes in terms of molecular structure, in parallel with physico-structural (SEM, TEM, AFM) and biological methods. In the longer view, with the development of new instrumentation, rapid spectropathological screening and classification of tendon damage in a clinical setting can be envisioned.

Veres and Lee first demonstrated the existence of nanoscale serial kinking in collagen fibrils within ruptured and cyclically overloaded tendons,[14] co-articulating what we now term the discrete plasticity mechanism as a protective mechanism in tendon biomechanics. Recently, the overload-induced collagen kink morphology was shown to be a possible cue to cellular recognition of injury.[34] FTIR PCI is eminently suitable to monitor fibril organization, particularly

with diffraction-limit optics that enable imaging at 1.1 μm pixel dimension, since this is a good match with natural fibril width. FTIR spectra provide molecular spectroscopic evidence of fibril orientation in control tendon, Fig. 1. Contrast is easily displayed, given the enormous difference in relative intensities of the amide I and II bands when the polarized infrared light is aligned either with the amide carbonyls (0°) or with the backbone (90°), as well as large differences in many of the other backbone modes.

In control tendon, fibrils are well organized; D-bands were clearly evident in SEM images (Fig. 2A), whereas mechanical overload introduced the expected serial nanoscale kinks characteristic of discrete plasticity (Fig. 2B and C). Some undulating crimps were easily seen in the visible images (Fig. 3A) and also in lower magnification SEM (not shown). Spectra extracted from a mosaic represent the typical variation that accompanies the undulating orientation of crimps in normal fibrils (Fig. 3B). Relative intensities are not directly comparable under different polarizations, but the FTIR PCI false colour scale in the processed images was adjusted to achieve the same, relatively narrow range of colour contrast, from yellow to blue (Fig. 3C and D) in control images. These ranges were optimized to allow for the full range observed in all tissues, including those that had been mechanically damaged.

In the mechanically damaged tendons, FTIR PCI revealed extreme alignment in uncrimped tendon fibrils in some cases, and an uneven loss of crimp, with concomitant molecular level disorder in others. The amide II band dominates in all spectra throughout the uncrimped region imaged in Fig. 4A, C and E. The calculated ratio for our chosen imaging parameters is consistently of the order of 1.7 to 2.0. Fibrils are visibly aligned; false colour FTIR images capture this alignment. The amide I band profile is well-known to be a good indicator of protein conformation. In normal self-assembled collagen, the typically observed profile is an asymmetric amide I band, with a maximum at around 1660 cm^{-1} and a lower energy shoulder at around 1635 cm^{-1}.[7–10] We note that spectral band shapes were unaltered from the norm and only the relative intensities had changed, indicating a high degree of physical order, but no evidence of denaturation.

Some of the spectral variations that were observed (Fig. 4B, D and F) suggested that despite their physical alignment, the fibrils were internally disorganized, *i.e.*, that nanoscale kinking had occurred. Undulations matching normal crimped tissue were evident in the lower part of these images. As before, the FTIR PCI results indicated fibre alignment without much nanoscale disorder in some regions where crimps were lost, seen here as yellow stripes in the false colour image Fig. 4D and yellow spectra in Fig. 4F. Interestingly, blue-green swaths were found between the yellow bands in Fig. 4D. In these regions, while the visible tissue image suggested that the crimps were lost and fibres were axially straightened, the amide II to amide I band area ratio was much lower than that expected for intact but well-ordered, aligned fibrils (Fig. 4F, blue and green spectra). In fact, the amide II band was frequently less intense than the amide I; the range of values for the amide II to amide I ratio was 0.9 to 1.2. Given the physical alignment of the fibre bundles with the polarization of the IR light, the most plausible explanation is that these regions underwent much greater, localized, tension, leading to significant kinking of fibrils within the fibre bundle.

Subsequent AFM surface imaging of these regions confirmed the existence of nanoscale kinking. AFM surface images of the well-aligned fibres in the visible image and FTIR PCI (Fig. 5A) show well-ordered fibrils with clear D-banding at the sub-micron scale, Fig. 5B and C. Light kinking is observed, corresponding to only a few kinks per $1.1 \times 1.1\ \mu m^2$ pixel area sampled by a high magnification FTIR field of view. As noted, the spectra in the FTIR PCI are nearly uniform throughout (Fig. 4E). From the AFM results, we may conclude that the massive amide II enhancement in axially aligned tendon indicates nearly linear orientation of well-organized fibrils. FTIR PCI gives molecular evidence that the stress was sufficient to eliminate the microscale waveform crimp that fibrils normally follow, but, with only a few kinks per pixel, did not produce sufficient molecular disorder to cause a change in the PCI spectra.

In stark contrast, the AFM surface images in Fig. 6 exhibit alternating regions of uncrimped fibrils (yellow strips in FTIR image Fig. 6A; upper AFM images in Fig. 6B and C) and regions of disordered fibrils and with nanokinks in regions with low polarization contrast (blue-green strips in FTIR image Fig. 6A; middle and lower AFM images in Fig. 6B and C). Together, the results in Fig. 5 and 6 show that in some cases, the mechanical damage was heterogeneous, producing higher stress leading to regions of disorder immediately adjacent to regions that experienced relatively lower stress, such that the crimp structure was regained upon release of the mechanical force. This might be an artefact arising from an uneven grip in the experimental mechanical damage procedure. However, it has recently been shown that interfibrillar shear stresses occur under notch tension testing of rat tail tendon.[35] Both uneven tension and natural variations in the tendon architecture may contribute to this result, though the degree to which each is involved remains a question yet to be resolved.

4.2 What does nanoscale near-field infrared imaging give us?

With the FTIR imaging at the 1.1 micron scale, fibril damage at the nanometer scale may be suspected but cannot be proved. The SINS experiment at BL 5.4.1 is the first synchrotron site in the world to combine the high chemical specificity of FTIR with the nanoscale spatial resolution of AFM.[20] This facility was designed on the same basic principles as the broad band DFG laser s-SNOM, in that both employ an asymmetric Michelson interferometer with the sample located under the AFM tip in the extended fixed-mirror arm of the interferometer.[21–24] The brilliant broad band source has greater source intensity, but must be tuned through three spectral ranges to get the entire mid-IR spectrum. With the QCL, a fibril may be scanned at a single wavelength; the relative absorbance at different wavelengths can be used to create spectral contrast images.

The results shown in Fig. 7 demonstrate that near-field IR gives the required nanoscale resolution to image fibrils and even to identify differences in optical response across the D-banding structure. Several important features can now be exploited. First, comparison of the absorbance spectra with those in Fig. 1 illustrates the importance of polarization: spectra have an enhanced amide I band, relative to the amide II and the backbone modes. Here, however, it is the orientation of the electric field, which is polarized parallel to the tip and to some of the amide carbonyl groups, which are perpendicular to the fibril lying on the slide, that causes the spectra to be the same as that in the far-field 0° polarization

spectrum.[23] While the far-field FTIR PCI experiments allowed us to evaluate polarization in the (x, y) plane of the tendon section, the near-field IR experiments allow us to evaluate polarization in the z-direction. The phenomenon is observed in both the synchrotron source and broad band source spectra, Fig. 7A. The absence of characteristic bands in the amide III region, especially those at 1337, 1284, 1240 and 1204 cm^{-1}, is understandable given that they are enhanced only for light polarized parallel to the fibril. From this, we can deduce that these other modes would become active if disorder caused the molecular backbone of fibrils to be aligned parallel to the tip.

The single wavelength images (Fig. 7B) present a dramatic example of the power of this technique for the study of oriented materials. The distinct D-band pattern is apparent in all of the images. The D-band defines a region that includes a gap between staggered tropocollagen molecules and the telopeptide sequences at the ends of the three individual chains in each triple helix.[15,32] Since the spectral contrast is based on the intensity of the carbonyl band, we can conclude that the amide group orientation is changing with local changes in molecular orientation down the length of the fibril. The D-band gap has been found to increase slightly under tension.[36] Although the contrast in the amplitude response is much lower than that of the phase response, the amplitude image is somewhat smoother. Since this is the first demonstration of a near-field nano-FTIR image of a single collagen fibril, and is taken only at two wavelengths, it is premature to speculate on the reasons for this difference in signal quality. Further work is planned to address these questions and to explore semi-quantitative analysis of the full spectral differences along the length of normal and damaged fibrils.

Band position is of interest, since different conformations might be anticipated in normal and in damaged tendon. Amide I and II band shapes and positions are sensitive to molecular conformation, thus, if disorder is at a molecular scale, *i.e.*, molecular denaturation, then we should also be able to see this in nearfield spectra. Subtle changes in molecular dynamics were detected with AFM-based nanomechanical mapping of single hydrated collagen fibrils at indentation speeds around 1 mm s^{-1}, at temperatures above 50 °C.[37] Using the same technique with overloaded fibrils, they have shown the presence of a poorly organized surface shell,[38] as seen in the many fibrils lacking D-banding in the SEM image presented here (Fig. 2C), and previously.[15] In this context, it will be critical to compare near-field IR results with the first surface and tip-enhanced Raman (SERS and TERS) analysis of the surface of collagen fibrils,[39] which showed the presence of different protein conformations at the surface of the fibrils. By permitting examination of polarization (orientation) dependence and band positions, near-field nano-FTIR thus opens the door into the spectroscopic evaluation of fibril structure at a molecular scale. This knowledge will be a unique window into what it means for soft tissues to be *damaged* in terms of structural change at the most fundamental level.

4.3 Potential and implications

With regard to the problem investigated here, the discrete plasticity response may be a fundamental feature of collagen's evolutionary design that helps to determine the remarkable toughness of connective tissues and the inflammatory and healing responses to injury. Spectropathological understanding of this key

structural feature of soft tissue injuries can serve the development of rational strategies for modulation of injury recognition and optimized healing. This particular health issue is one example of damage occurring in an ordered system, damage that is amenable to analysis with FTIR PCI at the micron scale. The hierarchical, oriented structure is typical of many collagen-based materials, as is the fact that disease may often be equated with disorder. In the case of tendon, a spatial resolution of 1 μm is fortuitously a good match for fibre dimension. The polarization-dependent nature of the IR spectra of collagen fibres was recognized at the dawn of FTIR microscopy.[1] With the spatial resolution capability of current commercial FTIR microscopes, this approach can be applied to the study of disease-induced disorder in a broad range of tissues from extracellular matrix to bone, to monitor disease state and healing, and to evaluate synthetic collagen matrices and scaffolds for bioengineered tissue replacements.

FTIR PCI spectropathology as presented here has been performed in transmission, on tendon sections mounted on relatively expensive salt windows. This is perceived as a necessity, *versus* the much less expensive transflectance substrates, notably the low-emissivity Keveley MirrIR substrates, which cost about 1% that of a BaF_2 window, because of the standing wave artefacts associated with transflectance spectra of thin sections.[40,41] Despite these artefacts, valid biomarkers for transflectance FTIR PCI have been identified in cartilage sections, though mineralized tissues were more problematic.[42] Provided that reference spectra are understood and samples are prepared consistently, the less expensive transflectance substrates could be a cost-effective option for tissue studies.

Infrared fibre optic probes have been used in the clinical evaluation of connective tissue,[43,44] with spectral results that show evidence of cartilage degeneration in surgically excised human tissue. The probe contact surface was a ZnS ATR crystal, 1 mm in diameter, and tissue grading was achieved through PLS analysis of some 150 spectra taken at different points. The classification was based on changes in several spectral parameters, but general tissue orientation could only be assessed in tissue sections imaged with a standard bench microscope and IR polarizer, at 6.25 μm pixel resolution.[44] Nevertheless, instrumental capabilities are evolving and it may eventually be possible to include polarization and tissue orientation as part of a clinical probe.

Near-field nanoscale infrared imaging capabilities are evolving swiftly, raising the question not of whether but of how such tremendously detailed information can be exploited for spectropathology. As seems evident from this work, the fact that the near-field nano-FTIR spectra are *z*-polarized is an important aspect that can be exploited in the study of the molecular basis of disease, particularly those diseases involving the formation or destruction of protein aggregates. The results of the experiments presented here demonstrate that we have the capability of studying the spectra of collagen fibrils at the level of their molecular organization. In future work, we will study the changes that occur at the fibril and molecular levels in mechanically damaged tendon. With near-field nano-FTIR, we hope to obtain confirmation that collagen molecules are locally denatured, perhaps *via* specific mechanisms, at specific sites within overload-damaged fibrils. In future work, we plan to explore the question of when and how this mechanism appears in the human life cycle, from youth to old age.

5. Conclusions

Collagen is the critical load-bearing constituent of mammals and performs innumerable functions throughout the body, all of which are enabled by the highly ordered structures that scale from molecular tropocollagen molecules and fibrils, up to fibres, fasicles, tendons and the matrices of bones and teeth. In tendon, cartilage, and certain other tissues, disorder may often be equated with damage and disease. The first high-magnification FTIR PCI spectra of control and mechanically damaged tendons show spectral differences in the relative intensity of the conformationally sensitive amide I and II bands. Different degrees of mechanical damage and disorder within individual tendons can be detected spectroscopically at the fibre length scale of 1 μm. SEM images of parallel matched-pair tendons confirm the presence of mechanical damage, in the form of serial kinking in collagen fibrils. AFM surface images of the sections imaged with FTIR PCI confirm the presence of fibril disorder and the presence of kinks at the nanoscale. With near-field nano-FTIR spectroscopy, it has been possible to obtain the first ever spatially resolved infrared spectra and images of collagen fibrils, including remarkably distinct spectral variations with D-bands. These techniques offer significant advantages for fundamental research, spectropathology and clinical applications.

Acknowledgements

This research is funded by a grant from the Canadian Institutes for Health Research, MOP-133453. S. Baldwin acknowledges the support of an ASPIRE CREATE NSERC PhD Fellowship; C. Findlay acknowledges the support of a Research Manitoba Health Studentship (PhD). The authors thank Reid's Meats, NS, Canada, for their assistance with the collection of tendon samples and Pat Scallion, Institute for Research in Materials at Dalhousie University for assistance with scanning electron microscopy. We are grateful to Dr Hans Bechtel and Dr Michael C. Martin for assistance with data collection at Beam Line 5.4.1 at the Advanced Light Source, Berkeley CA, USA. The authors are very grateful to Neaspec GmbH DE, and in particular to Dr Max Eisele of Neaspec, for the nano-FTIR spectra and the phase and amplitude-resolved near-field images of collagen fibrils and for many helpful discussions.

References

1 R. D. B. Fraser, *Discuss. Faraday Soc.*, 1950, **9**, 379–383.
2 R. M. Badger and A. D. E. Pullin, *J. Chem. Phys.*, 1954, **22**, 1142.
3 J. T. Randall, R. D. B. Fraser, S. Jackson, A. V. W. Martin and A. C. T. North, *Nature*, 1952, **169**, 1029–1033.
4 F. O. Schmitt, *Proc. Am. Philos. Soc.*, 1956, **100**, 476–486.
5 A. J. Hodge and F. O. Schmitt, *Proc. Natl. Acad. Sci. U. S. A.*, 1960, **46**, 186–197.
6 P. Fratzl, K. Misof, I. Zizak, G. Rapp, H. Amenitsch and S. Bernstorff, *J. Struct. Biol.*, 1998, **122**, 119–122.
7 K. Esmonde-White, *Appl. Spectrosc.*, 2014, **68**, 1203–1218.

8 C. Eklouh-Molinier, T. Happillon, N. Bouland, C. Fichel, M.-D. Diébold, J.-F. Angiboust, M. Manfait, S. Brassart-Pasco and O. Piot, *Analyst*, 2015, **140**, 6260–6268.
9 A. Boskey and N. P. Camacho, *Biomaterials*, 2007, **28**, 2465–2478.
10 R. Wiens, M. Rak, N. Cox, S. Abraham, B. H. J. Juurlink, W. M. Kulyk and K. M. Gough, *Anal. Bioanal. Chem.*, 2007, **387**, 1679–1689.
11 A. Masic, L. Bertinetti, R. Schuetz, S.-W. Chang, T. H. Metzger, M. J. Buehler and P. Fratzl, *Nat. Commun.*, 2015, **6**, 5942.
12 N. S. Kalson, Y. Lu, S. H. Taylor, T. Starborg and D. F. Holmes, *eLife*, 2015, DOI: 10.7554/eLife.05958.001.
13 B. Brodsky and A. V. Persikov, *Adv. Protein Chem.*, 2005, **70**, 301–339.
14 S. P. Veres and J. M. Lee, *Biophys. J.*, 2012, **102**, 2876–2884.
15 S. P. Veres, J. M. Harrison and J. M. Lee, *J. Orthop. Res.*, 2013, **31**, 731–737.
16 S. P. Veres, J. M. Harrison and J. M. Lee, *Matrix Biol.*, 2014, **33**, 54–59.
17 M. J. Nasse, M. J. Walsh, E. C. Mattson, R. Reininger, A. Kajdacsy-Balla, V. Macias, R. Bhargava and C. J. Hirschmugl, *Nat. Methods*, 2011, **8**, 413–416.
18 C. R. Findlay, R. Wiens, M. Rak, J. Sedlmair, C. J. Hirschmugl, J. Morrison, C. J. Mundy, M. Kansiz and K. M. Gough, *Analyst*, 2015, **140**, 2493–2503.
19 R. K. Reddy, M. J. Walsh, M. V. Schulmerich, P. S. Carney and R. Bhargava, *Appl. Spectrosc.*, 2013, **67**, 93–105.
20 H. A. Bechtel, E. A. Muller, R. L. Olmon, M. C. Martina and M. B. Raschke, *Proc. Natl. Acad. Sci. U. S. A.*, 2014, **111**, 7191–7196.
21 T. Taubner, R. Hillenbrand and F. Keilmann, *Appl. Phys. Lett.*, 2004, **85**, 5064–5066.
22 F. Huth, A. Govyadinov, S. Amarie, W. Nuansing, F. Keilmann and R. Hillenbrand, *Nano Lett.*, 2012, **12**, 3973–3978.
23 I. Amenabar, S. Poly, W. Nuansing, E. H. Hubrich, A. A. Govyadinov, F. Huth, R. Krutokhvostov, L. Zhang, M. Knez, J. Heberle, A. M. Bittner and R. Hillenbrand, *Nat. Commun.*, 2013, **4**, 1–9.
24 S. Mastel, A. A. Govyadinov, T. V. A. G. de Oliveira, I. Amenabar and R. Hillenbrand, *Appl. Phys. Lett.*, 2015, **106**, 023113.
25 D. M. Stitt, M. Z. Kastyak-Ibrahim, C. R. Liao, J. Morrison, B. Albensi and K. M. Gough, *Vib. Spectrosc.*, 2012, **60**, 16–22.
26 W. H. Moore and S. Krimm, *Biopolymers*, 1976, **15**, 2439–2464.
27 G. S. Young, *Mater. Res. Soc. Symp. Proc.*, 1992, **267**, 859–867.
28 N. P. Camacho, P. West, P. A. Torzilli and R. Mendelsohn, *Biopolymers*, 2001, **62**, 1–8.
29 M. D. Shoulders and R. T. Raines, *Annu. Rev. Biochem.*, 2009, **78**, 929–958.
30 B. B. Doyle, D. W. L. Hukins, D. J. S. Hulmes, A. Miller, C. J. Rattew and J. Woodhead-Galloway, *Biochem. Biophys. Res. Commun.*, 1974, **60**, 858–864.
31 J. P. R. O. Orgel, T. C. Irving, A. Miller and T. J. Wess, *Proc. Natl. Acad. Sci. U. S. A.*, 2006, **103**, 9001–9005.
32 M. J. Buehler, *Proc. Natl. Acad. Sci. U. S. A.*, 2006, **103**, 12285–12290.
33 M. J. Tobin, M. A. Chesters, J. M. Chalmers, F. J. M. Rutten, S. E. Fisher, I. M. Symonds, A. Hitchcock, R. Allibone and S. Dias-Gunasekara, *Faraday Discuss.*, 2004, **126**, 27–39.
34 S. P. Veres, E. P. Brennan-Pierce and J. M. Lee, *J. Biomed. Mater. Res., Part A*, 2015, **103**, 397–408.

35 S. E. Szczesny, J. L. Caplan, P. Pedersen and D. M. Elliott, *Sci. Rep.*, 2015, **5**, 14649–14658.
36 M. P. E. Wenger and P. Mesquida, *Appl. Phys. Lett.*, 2011, **98**, 163707.
37 S. J. Baldwin, A. S. Quigley, C. Clegg and L. Kreplak, *Biophys. J.*, 2014, **107**, 1794–1801.
38 S. J. Baldwin, in prep.
39 C. Gullekson, L. Lucas, K. Hewitt and L. Kreplak, *Biophys. J.*, 2011, **100**, 1837–1845.
40 P. Bassan, A. Sachdeva, A. Kohler, C. Hughes, A. Henderson, J. Boyle, J. H. Shanks, M. Brown, N. W. Clarke and P. Gardner, *Analyst*, 2012, **137**, 1370–1377.
41 J. Filik, M. D. Frogley, J. K. Pijanka, K. Wehbe and G. Cinque, *Analyst*, 2012, **137**, 853–861.
42 A. Hanifi, C. McGoverin, Y.-T. Oua, F. Safadi, R. G. Spencer and N. Pleshko, *Anal. Chim. Acta*, 2013, **779**, 41–49.
43 A. Hanifi, H. McCarthy, S. Roberts and N. Pleshko, *PLoS One*, 2013, **8**, e64822.
44 A. Hanifi, X. Bi, B. Kavukcuoglu, P. C. Lin, E. DiCarlo, R. G. Spencer, M. P. G. Bostrom and N. Pleshko, *Am. J. Sports Med.*, 2012, **40**, 2853–2861.